ClinicSearch

Clinical Trials and Clinical Research

Delia Teresa Sponza *

Open Access

Research Article

Photocatalytic Removal of Carbamazepine Via Tio2/Ti3c2tx (Mxene) Nanocomposite

Rukiye Öztekin, Delia Teresa Sponza*

Dokuz Eylül University, Engineering Faculty, Department of Environmental Engineering, Tınaztepe Campus, 35160 Buca/Izmir, Turkey.

***Corresponding Author:** Delia Teresa Sponza, Dokuz Eylül University, Engineering Faculty, Department of Environmental Engineering, Tınaztepe Campus, 35160 Buca/Izmir, Turkey.

Received Date: 31 October, 2023; **Accepted Date:24 November, 2023; Published Date: 30 November, 2023**

Citation: Öztekin R., Delia T. Sponza, (2023), Effect of Traditional Moxibustion in Assisting the Rehabilitation of Stroke Patients, *Clinical Trials and Clinical Research.* 2(6); **DOI:**10.31579/2834-5126/040

Abstract

In this study, a novel titatium dioxide/titanium carbide (MXene) heterostructure nanocomposites (TiO2/Ti3C2Tx NCs) was examined during photocatalytic degradation process (PCD) in the efficient removal of carbamazepine (CBZ) antiepileptic drug in pharmaceutical industry wastewater (PCI ww), İzmir, Turkey. Different pH values (3.0, 4.0, 5.0, 6.0, 7.0, 9.0 and 11.0), increasing photodegradation times (30, 60, 90, 120, 150 and 180 min), increasing CBZ concentrations (5, 10, 15 and 20 mg/l) and increasing TiO2/Ti3C2Tx MXene heterostructure NCs concentrations (5, 10, 20, 40 and 80 mg/l) was operated during PCD for the efficient removal of CBZ in PCI ww. The characteristics of the synthesized nanoparticles (NPs) were assessed using XRD, RS, XPS, FESEM, FTIR and TEM analyses, respectively. ANOVA statistical analysis was used for all experimental samples. The maximum 99.34%% CBZ removal was obtained after PCD in PCI ww, at pH=5.0, at 300 W UV-vis and at 25oC, respectively. 99.58% CBZ maximum removal was observed after 180 min with PCD in PCI ww, at 300 W UV-vis, at pH=5.0 and at 25oC, respectively. The maximum 99.42% CBZ removal was obtained at 10 mg/l CBZ with PCD in PCI ww after 180 min, at 300 W UV-vis, at pH=5.0 and at 25oC, respectively. The maximum 99.67% CBZ removal was obtained at 10 mg/l TiO2/Ti3C2Tx MXene heterostructure NCs, after 180 min, at 10 mg/l CBZ, at 300 W UV-vis, at pH=5.0 and at 25oC, respectively. Finally, the combination of a simple, easy operation preparation process, cost effective and excellent performance makes this a novel TiO2/Ti3C2Tx MXene heterostructure NCs a promising option during PCD for the removals of CBZ antiepileptic drugs in PCI ww treatment.

Keywords: anova statistical analysis; carbamazepine (cbz); pharmaceutical industry wastewater; photocatalytic degradation process; tio2/ti3c2tx (mxene) nanocomposite

1. Introduction

Pharmaceutical industry is one of the important and largest industries worldwide and at the same time, a large number of contaminations is being generated by the pharmaceutical products. These products are largely disbursed at high quantities into the environment by purposely and accidentally. As a result, pharmaceutical compounds can be found in different environmental compartments such as soil, water surfaces, and even in drinking water. Specially, pharmaceutical products are frequently detected in natural and wastewater system [1, 2]. The number of pharmaceutical pollutants and their metabolites collection in water bodies are not high-pitched (ng/l to mg/l), however, these pharmaceutical molecules are specifically designed to initiate the biological response at very low concentration levels. Therefore, it may lead to some adverse effects on biological system and human health such as aquatic toxicity, high resistance bacteria, acute and chronic disease, hormonal and endocrine disruption. Moreover, most of the pharmaceutical drugs possess very stable chemical structure and non-biodegradable properties. Thus, the detection and removal/degradation of pharmaceutical compounds in the water system has been evolved as a growing concern in worldwide, which is essentially due to their potential toxicity and hazardous to the living ecosystems and human beings [3].

The various available techniques to remove and degrade the water/wastewater contaminating pharmaceutical pollutants include adsorption, microbial degradation, photocatalysis, ozonolytic, electrocatalysis and membrane filtration processes [3, 4]. Of these techniques, the photocatalysis offers a promising solution for the effective degradation of antibiotics contaminants in water using solar energy [3, 5-7], where the strong redox reactions of photocatalysis offer effective mineralization, high degradation efficiency, less byproducts and/or simple/non-toxic degradation products. However, the photocatalytic efficiency of photocatalysts mainly depends upon many crucial features such as suitable band edge position, narrow band gap energy, reduced charge recombination, enhanced charge separation, transfer and surface-active sites [7]. Accordingly, considerable efforts have been made to achieve these properties by constructing hybrid nanocomposite structures of photocatalysts with controlled preparation methods [8]. As described, these hybrid nanocomposites fundamentally offer enhanced surface and

catalytic properties delivered by large surface area, rich active sites, extended photoabsorbance, higher charge generation, improved interfacial charge separation and strong redox properties [5, 6, 8, 9].

Carbamazepine (CBZ; C15H12N2O), is an antiepileptic drug currently prescribed for treatment of seizure disorders, chronic pain, and for psychopharmacotherapy [10], which is commonly found in environmental matrices (irrigation water, domestic wastewater and river water); It is very resistant to microbial biodegradation [11]. Usually, CBZ is excreted with <3% remaining in its unaltered form and flushed directly to the wastewater treatment plants (WWTPs) through the sewage system. Studies have determined that CBZ is persistent, with removal efficiencies by the WWTPs are being mostlybelow 10%. In the classification scheme for pharmaceutical biodegradation, CBZ has the status of "no-removal" [12]. Clara et al. [13], and Kosjek et al. [14], reported that CBZ is resistant to biodegradation and shows almost no elimination during conventional wastewater treatment. In order to completely remove the CBZ antiepileptic drug from the aquatic environment; There is a need for better and safer methods. In the removal of CBZ from the aquatic environment; Various treatment methods such as adsorption, chemical precipitation, ozonation, biofiltering and photocatalytic degradation are used [15]. The photocatalytic degradation is one of the best options for treating drinking water and wastewater streams contaminated with pharmaceuticals [16].

TiO2, a nano photocatalyst, is one of the most widely used photocatalysts to break down pharmaceutical pollutants in water [11, 17]. Leaf-shaped TiO2 has different phases; Theoretical studies combined with experimental studies have shown that the {0 0 1} side of anatase TiO2 is more reactive than the {1 0 1} side so that it can be excited by light [18, 19]. It has also been reported that the bonding of (0 0 1)-TiO2 to a 2-D material can reduce the band gap and increase the photocatalytic activity [20]. Ti3C2 contains a large amount of Ti, which can be easily converted to TiO2 by oxidation [21-24]. Ti3C2 can produce {0 0 1} anatase TiO2 facets in its nano-thin layers under certain conditions [19, 25]. The main limitation of TiO2 is a relatively wide band gap, (3.02 eV for rutile, 3.2 eV for anatase) which results in about 5% spectral overlap between its absorbance and sunlight emission ($\lambda < \sim 390$ nm) [26]. The most important disadvantages of TiO2 in the photocatalytic degradation process are; fast recombination of electron holes and low quantum yield [27]. In order to slow down the electron hole recombination rate; more research is needed. To reduce the band gap and for a photocatalyst with semiconductor heterojunctions; The modifications of TiO2 and the use of heterostructure nanocompounds with other chemical compounds provide higher yields [5].

Titanium carbide (Ti3C2Tx) MXenes are two-dimensional (2-D) carbide materials with layered stacking structure similar to graphene [28]. In 2011, Ti3C2Tx MXenes were first reported by Gogotsi [29]. This work opens the door to the preparation and application of 2-D MXenes. Then more and more researches have focused on the synthesis, properties, and applications of Ti3C2Tx MXenes [30]. The general formula of MXenes is Mn+1XnTx, where M is transition metal, such as Ti, Mo, Nb, V, Cr, Zr, Ta, etc., X is carbon, nitrogen (n = 1–4), and T is the surface-functionalized groups. MXenes exhibit high electrical conductivity (up to 20,000 S/cm) [31], high stability, superior mechanical properties, and tunable layered structure.

MXenes have attracted increasing interest and become the focus of researchers. There are wide potential applications in batteries, supercapacitors, solar cells and solar steam generation, electromagnetic interference (EMI) shielding materials [32-39]. MXenes have photocatalytic properties [40]. Various MXenes have been discovered in a number of research areas, including wastewater treatment [41, 42]. Titanium carbide (Ti3C2) MXene nanolayers are the first member of the MXene family [29], and retain their catalytic properties [40, 43]. Possible modifications and functionalizations of Ti3C2 make it a promising photocatalyst for CBZ degradation in aquatic environments. These advantages make MXene an attractive platform for preparing composites in photocatalytic systems [44]. In particular, Ti3C2Tx contains a large proportion of Ti, which can undergo surface oxidation to yield TiO2/ Ti3C2Tx [21-24]. Shahzad et al. [23], fabricated an anatase TiO2/Ti3C2Tx heterostructure through the hydro thermal treatment process, demonstrating an excellent photocatalytic degradation of the antiepileptic drug carbamazepine. More importantly, the interfacial Schottky junction that is formed between the TiO2 and the layered C atoms provides a large reservoir of holes, which facilitates the charge separation and transfer, essential for the formation of radicals involved in the photodegradation process [23].

In this study, TiO2/Ti3C2Tx MXene heterostructure NCs was examined during PCD in the efficient removal of CBZ in PCI ww, İzmir, Turkey. Different pH values (3.0, 4.0, 5.0, 6.0, 7.0, 9.0 and 11.0), increasing photodegradation times (30, 60, 90, 120, 150 and 180 min), increasing CBZ concentrations (5, 10, 15 and 20 mg/l) and increasing TiO2/Ti3C2Tx MXene heterostructure NCs concentrations (5, 10, 20, 40 and 80 mg/l) was operated during PCD for the efficient removal of CBZ in PCI ww. The characteristics of the synthesized NPs were assessed using XRD, RS, XPS, FESEM, FTIR and TEM analyses, respectively. ANOVA statistical analysis was used for all experimental samples.

2. Materials and Methods

2.1. Characterization of PCI WW

Characterization of the biological aerobic activated sludge proses from a PCI ww plant, İzmir, Turkey was performed. The results are given as the mean value of triplicate samplings (Table 1).

Parameters	Unit	Concentrations
Chemical oxygen demand-total (COD_{total})	(mg/l)	4000
Chemical oxygen demand-dissolved ($COD_{dissolved}$)	(mg/l)	3200
Biological oxygen demand-5 days (BOD_5)	(mg/l)	1500
BOD_5 / $COD_{dissolved}$		0.5
Total organic carbons (TOC)	(mg/l)	1800
Dissolved organic carbons (DOC)	(mg/l)	1100
pH		8.3
Salinity as Electrical conductivity (EC)	(mS/cm)	1552
Total alkalinity as $CaCO_3$	(mg/l)	750
Total volatile acids (TVA)	(mg/l)	380
Turbidity (*Nephelometric Turbidity unit, NTU)*	NTU	7.2
Color	1/m	50
Total suspended solids (TSS)	(mg/l)	250
Volatile suspended solids (VSS)	(mg/l)	187
Total dissolved solids (TDS)	(mg/l)	825
Nitride (NO_2^-)	(mg/l)	1.7
Nitrate (NO_3^-)	(mg/l)	1.91
Ammonium (NH_4^+)	(mg/l)	2.3
Total Nitrogen (Total-N)	(mg/l)	3.2

Sulfite ion (SO_3^{-2})	(mg/l)	21.4
Sulphate (SO_4^{-2})	(mg/l)	29.3
Chloride (Cl^-)	(mg/l)	37.4
Bicarbonate (HCO_3^-)	(mg/l)	161
Phosphate (PO_4^{-3})	(mg/l)	16
Total Phosphorus (Total-P)	(mg/l)	40
Total Phenols	(mg/l)	70
Oil & Grease	(mg/l)	220
Cobalt (Co^{+3})	(mg/l)	0.2
Lead (Pb^{+2})	(mg/l)	0.4
Potassium (K^+)	(mg/l)	17
Iron (Fe^{+2})	(mg/l)	0.42
Chromium (Cr^{+2})	(mg/l)	0.44
Mercury (Hg^{+2})	(mg/l)	0.35
Zinc (Zn^{+2})	(mg/l)	0.11

Table 1: Characterization of PCI ww.

2.2. Preparation of TiO2/Ti3C2Tx (MXene) NCs

For the synthesis of {0 0 1} facets of Ti3C2/TiO2 photocatalyst (001-T/MX); After mixing 200 mg of synthesized Ti3C2Tx powder and 0.330 g of NaBF4 (99%, Sigma-Aldrich) for 30 minutes, ultrasonication was applied for 10 minutes. 100 ml of Suspension was taken and kept in a teflon lined stainless steel autoclave at 160°C for 12 h. The sample was then washed several times with ethyl alcohol/deionised water until a pH=6.5 was reached. The as-synthesised photocatalyst was then dried in a vacuum oven at 70°C overnight and stored in a plastic jar until use.

2.3. Photocatalytic Degradation Reactor

A 2-liter cylinder quartz glass reactor was used for the photodegradation experiments in the PCI ww at different operational conditions. 1000 ml PCI ww was filled for experimental studies and the photocatalyst were added to the cylinder quartz glass reactors. The 300 W Xe lamp for UV-A vis light were placed to the outside of the photo-reactor with a distance of 3 mm. The photocatalytic reactor was operated with constant stirring (1.5 rpm) during the PCD. 10 ml of the reacting solution (10 mg/l CBZ solution and 10 mg/l TiO2/Ti3C2Tx MXene) were sampled and centrifugated (at 10000 rpm) at different time intervals at 25oC. The UV irradiation treatments were created using six 50 W Xe lamp for UV-A vis light (Total: 300 W) emitting in the 250–450 nm range (λmax = 350 nm; AM 1.5G filter, 100 mW/ cm2, FWHM = 17 nm; Actinic BL TL-D 18W, Philips). At given different photocatalytic degradation time intervals, the suspension of 10 ml was sampled and separated by centrifuge, then analyzed according to the absorbance at λmax >290 nm nm for CBZ by a UV-vis spectrometer (Cary 5000 UV-Vis Spectrophotometer from Varian, Siemens, Germany).

2.4. Characterizations

2.4.1. X-Ray Diffraction (XRD) Analysis

Powder XRD patterns were recorded on a Shimadzu XRD-7000, Japan diffractometer using Cu Kα radiation (λ = 1.5418 Å, 40 kV, 40 mA) at a scanning speed of 1o /min in the 10-80o 2θ range.

2.4.2. Raman Spectrophotometer (RS) Analysis

Raman spectrum was collected with a Horiba Jobin Yvon-Labram HR UV-Visible NIR (200-1600 nm) Raman microscope spectrometer, using a laser with the wavelength of 512 nm. The spectrum was collected from 10 scans at a resolution of 2 /cm. The zeta potential was measured with a SurPASS Electrokinetic Analyzer (Austria) with a clamping cell at 300 mbar.

2.4.3. X-Ray Photoelectron Spectroscopy (XPS) Analysis

XPS spectra were measured on a SPECS spectrometer equipped with a Phoibos 150 9MCD detector using a non-monochromatic X-ray source (Al and Mg) operating at 200 W. The samples were evacuated in the prechamber of the spectrometer at 1x10−9 mbar. The measured intensity ratios of the components were obtained from the area of the corresponding peaks after nonlinear Shirley-type background subtraction and corrected by the transition function of the spectrometer.

2.4.4. Field Emission Scanning Electron Microscopy (FESEM) Analysis

The morphological features and structure of the synthesized catalyst were investigated by FESEM (FESEM, Hitachi S-4700).

2.4.5. Fourier Transform Infrared Spectroscopy (FTIR) Analysis

The FTIR spectra of samples was recorded using the FT-NIR spectroscope (RAYLEIGH, WQF-510).

2.4.6. Transmission Electron Microscopy (TEM) Analysis

The structure of the samples was analyzed TEM analysis. TEM analysis was recorded in a JEOL JEM 2100F, Japan under 200 kV accelerating voltage. Samples were prepared by applying one drop of the suspended material in ethanol onto a carbon-coated copper TEM grid, and allowing them to dry at 25oC.

2.5. Analytical Procedures

CODtotal, CODdissolved, Total-P, PO4-3-P, Total-N, NH4+-N, NO3--N, NO2--N, BOD5, pH, T[(oC)], TSS, TVSS, TOC, Oil, Cl-, total phenol, TVA, DOC, total alkalinity, turbidity, TDS, color, SO3-2, SO4-2, HCO3-, salinity, Co+3, Pb+2, K+, Fe+2, Cr+2, Hg+2 and Zn+2 were measured according to the Standard Methods (2017) 5220B, 5220D, 4500-P, 4500-PO4-3, 4500-N, 4500-NH4+, 4500-NO3-, 4500-NO2-, 5210B, 4500-H+, 2320, 2540D, 2540E, 5310, 5520, 4500-Cl-, 5530, 5560B, 5310B, 2320, 2130, 2540E, 2120, 4500-SO3-2, 4500-SO4-2, 5320, 2520, 3500-Co+3, 3500-Pb+2, 3500- K+, 3500-Fe+2, 3500-Cr+2, 3500- Hg+2, 3500-Zn+2, respectively [45].

Total-N, NH4+-N, NO3--N, NO2--N, Total-P, PO4-3-P, total phenol, Co+3, Pb+2, K+, Fe+2, Cr+2, Hg+2, Zn+2, SO3-2, and SO4-2 were measured with cell test spectroquant kits (Merck, Germany) at a spectroquant NOVA 60 (Merck, Germany) spectrophotometer (2003).

The measurement of color was carried out following the methods described by Olthof and Eckenfelder [46], and Eckenfelder [47]. According these methods, the color content was determined by measuring the absorbance at three wavelengths (445 nm, 540 nm and 660 nm), and taking the sum of the absorbances at these wavelengths. In order to identify the color in 25 ml PCI ww was acidified at pH=2.0 with a few drops of 6 N HCl and extracted three times with 25 ml of ethyl acetate. The pooled organic phases were dehydrated on sodium sulphate, filtered and dried under vacuum. The residue was sylilated with bis(trimethylsylil)trifluoroacetamide (BSTFA) in dimethylformamide and analyzed by gas chromatography–mass spectrometry (GC-MS) and gas chromatograph (GC) (Agilent Technology model 6890N) equipped with a mass selective detector (Agilent 5973 inert MSD). Mass spectra were recorded using a VGTS 250 spectrometer equipped with a capillary SE 52

column (HP5-MS 30 m, 0.25 mm ID, 0.25 µm) at 220°C with an isothermal program for 10 min. The initial oven temperature was kept at 50oC for 1 min, then raised to 220oC at 25oC/min and from 200 to 300oC at 8oC/min, and was then maintained for 5.5 min. High purity He (g) was used as the carrier gas at constant flow mode (1.5 ml/min, 45 cm/s linear velocity).

The total phenol was monitored as follows: 40 ml PCI ww was acidified to pH=2.0 by the addition of concentrated HCl. Total phenol was then extracted with ethyl acetate. The organic phase was concentrated at 40°C to about 1 ml and silylized by the addition of N, O-bis(trimethylsilyl) acetamide (BSA). The resulting trimethylsilyl derivatives were analysed by GC-MS (Hewlett-Packard 6980/HP5973MSD).

Methyl tertiary butyl ether (MTBE) was used to extract oil from the water and NPs. GC-MS analysis was performed on an Agilent gas GC system. Oil concentration was measured using a UV–vis spectroscopy fluorescence spectroscopy and a GC–MS (Hewlett-Packard 6980/HP5973MSD). UV–vis absorbance was measured on a UV–vis spectrophotometer (Cary 5000 UV-Vis Spectrophotometer from Varian, Siemens, Germany), and oil concentration was calculated using a calibration plot which was obtained with known oil concentration samples.

2.6. Statistical Analysis

ANOVA analysis of variance between experimental data was performed to detect F and P values. The ANOVA test was used to test the differences between dependent and independent groups [48]. Comparison between the actual variation of the experimental data averages and standard deviation is expressed in terms of F ratio. F is equal (found variation of the date averages/expected variation of the date averages). P reports the significance level, and d.f indicates the number of degrees of freedom. Regression analysis was applied to the experimental data in order to determine the regression coefficient R2, [49]. The aforementioned test was performed using Microsoft Excel Program.

All experiments were carried out three times and the results are given as the means of triplicate samplings. The data relevant to the individual pollutant parameters are given as the mean with standard deviation (SD) values.

3. Results and Discussions

3.1. The Photocatalytic Degradation Mechanism of TiO2/Ti3C2T NCs

TiO2 for mineralization of organic micropollutants by oxidation process under UV-vis light radiation; It is one of the most widely used photocatalysts. TiO2 forms vacancies (h+) and electrons (e−1), which react with water molecules and produce active radicals [5]. Under UV-vis light irradiation, exposed {0 0 1} facets of TiO2 excited and produced e−1 and h+, which then reacted with dissolved oxygen to form reactive OH● radicals. Ti3C2Tx carries OH as a surface functional group in the form of Ti−C−O [50]. After controlled oxidation to form heterojunctions, Ti3C2Tx was terminated by OH groups; It exhibits metallic behavior with its narrow band and carrier mobility [29]. (0 0 1)-TiO2-Ti3C2Tx in the electron transfer mechanism in heterojunctions; The transfer of electrons generated on the TiO2 surface to the Ti3C2Tx layers at the interface is prevented. There are likely two reasons for this: (1) Ti3C2Tx has a higher negative Fermi level than TiO2's conduction band; because the charge transfer resistance depends on the Fermi levels of the surface states and conduction band [51]; and (2) the work function of Ti3C2Tx is much lower than that of TiO2. In a theoretical working calculation, OH-terminated Ti3C2Tx nanosheets (1.8 eV) have a much lower work function than (0 0 1)-TiO2 (4.924 eV) [52]. Considering the large gap in the work function of the two phases in the heterostructure through their interface, the Schottky barrier has been estimated [43]. The Schottky barrier is a potential energy barrier for electrons formed in a metal semiconductor; It can inhibit electron transfer from TiO2 to Ti3C2Tx, but allow h+ flow to the photogenerate. The Schottky barrier effectively prevents the backflow of h+ through the TiO2-Ti3C2Tx interface.

3.2. The Degradation Pathways of CBZ

Possible photocatalytic degradation pathways of CBZ; The aromatic ring of CBZ was attacked by OH● free radicals generated from the photocatalyst's heterojunctions, producing a stable intermediate followed by H-abstraction. According to the detected intermediates, path 1 and path 2; Two different degradation pathways are proposed [53]. In pathway 1, the OH● substitution in the CBZ molecule can produce hypothetical intermediates I, II, and III; then ring cleavage produces two degradation products, designated A (2-hydroxybenzoic acid) and B (2-aminobenzoic acid) (Figure 1).

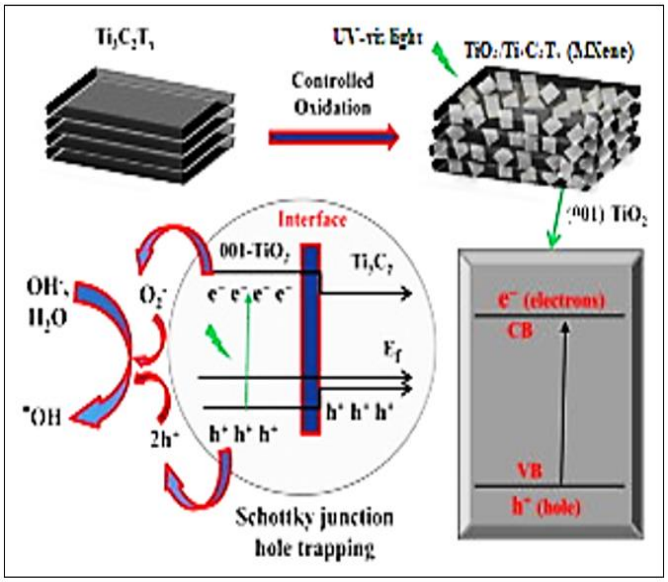

Figure 1: The Degradation Pathways of CBZ.

In Path 2, the substitution of O● in hypothetical intermediate I produces hypothetical intermediates IV and then V; It consists of the identified intermediate C (acridine) (Figure 1). More OH● substitutions than acridine form intermediate D, defined as formaldehyde-acridine. As a result of more transformations in pathway 1, more oxidation and ring cleavage; It can produce aniline and benzoic acid, which is reduced to CO2 and H2O [54]. However, in route 2, formaldehyde-acridine (intermediate D) was converted to CO2 and H2O by ring cleavage processes (Figure 1).

3.3. Characterizations

3.3.1. The Results of XRD Analysis

The results of XRD analysis of as prepared for TiO2 NPs (Figure 2a), Ti3C2Tx NCs (Figure 2b) and TiO2/Ti3C2Tx MXene heterostructure NCs (Figure 2c), respectively, after PCD of CBZ in PCI ww (Figure 2). The characterization peaks of TiO2 NPs were observed at 2θ values and corresponding of 9.41o (004), 33.17o (112), 37.24o (006), 39.71° (104), 42.87o (020) and 61.09o (008), respectively (Figure 2a). The XRD patterns of Ti3C2Tx NCs showed the 2θ values and corresponding of 9.58° (103), 18.64° (202), 28.17o (112), 34.40o (008), 35.63° (133), 38.16o (110), 42.28o (200) and 62.23o (301), respectively (Figure 2b). The XRD peaks of TiO2/Ti3C2Tx MXene heterostructure NCs obtained at 2θ values and corresponding of 25.38o (100), 38.12o (302), 48.27o (101), 55.12o (110), 56.28o (204) and 64.33o (113), respectively (Figure 2c).

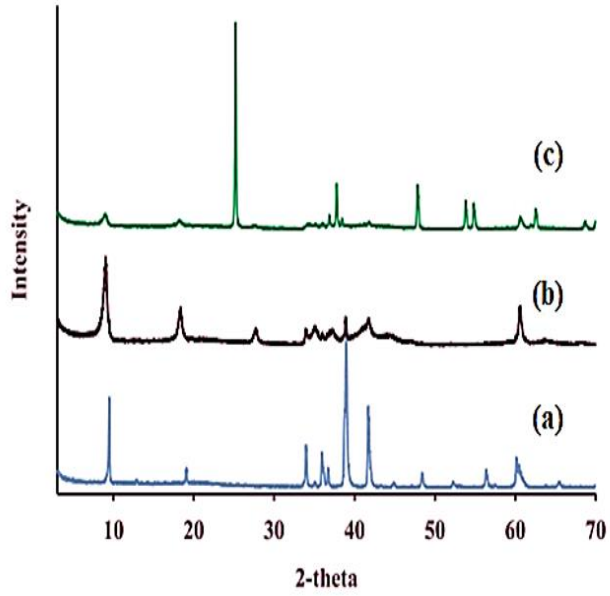

Figure 2: The XRD spectra of (a) TiO2 NPs, (b) Ti3C2Tx NCs and (c) TiO2/Ti3C2Tx MXene heterostructure NCs, respectively, after PCD of CBZ in PCI ww.

3.3.2. The Results of RS Analysis

The results of RS analysis of as prepared for Ti3C2Tx NCs (Figure 3a) and TiO2/Ti3C2Tx MXene heterostructure NCs (Figure 3b) after PCD of CBZ in PCI ww (Figure 3). The RS patterns of Ti3C2Tx NCs observed the 2θ values and corresponding of 100.12° (101) and 558.74o (201), respectively (Figure 3a). The RS peaks of TiO2/Ti3C2Tx MXene heterostructure NCs obtained at 2θ values and corresponding of 175.12o (120), 400.28o (211), 512.10o (320) and 645.73o (103), respectively (Figure 3b).

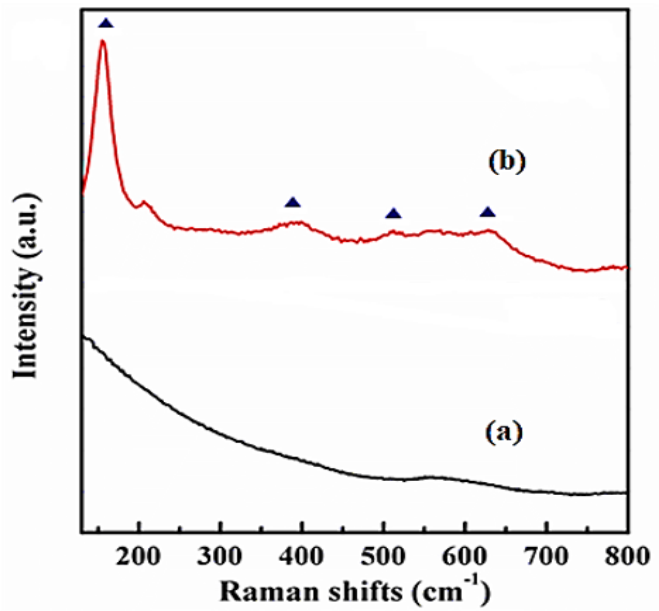

Figure 3: The RS spectra of (a) Ti3C2Tx NCs and (b) TiO2/Ti3C2Tx MXene heterostructure NCs after PCD of CBZ in PCI ww (▲: TiO2 NPs).

3.3.3. The Results of XPS Analysis

The XPS images of TiO2/Ti3C2Tx MXene heterostructure NCs was observed after PCD of CBZ in PCI ww (Figure 4).

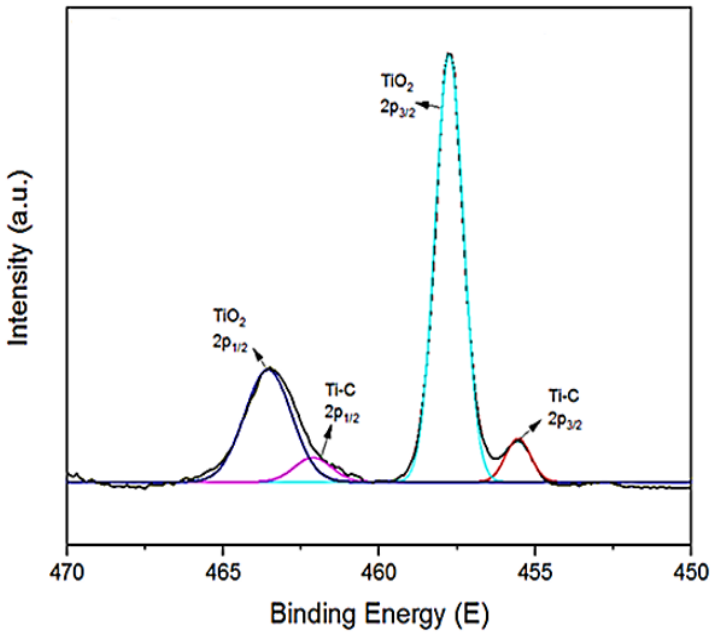

Figure 4: The XPS spectra of TiO2/Ti3C2Tx MXene heterostructure NCs after PCD of CBZ in PCI ww**.**

3.3.4. The Results of FESEM Analysis

The morphological features of TiO2/Ti3C2Tx MXene heterostructure NCs were characterized through FESEM images (Figure 5) after PCD of CBZ in PCI ww.

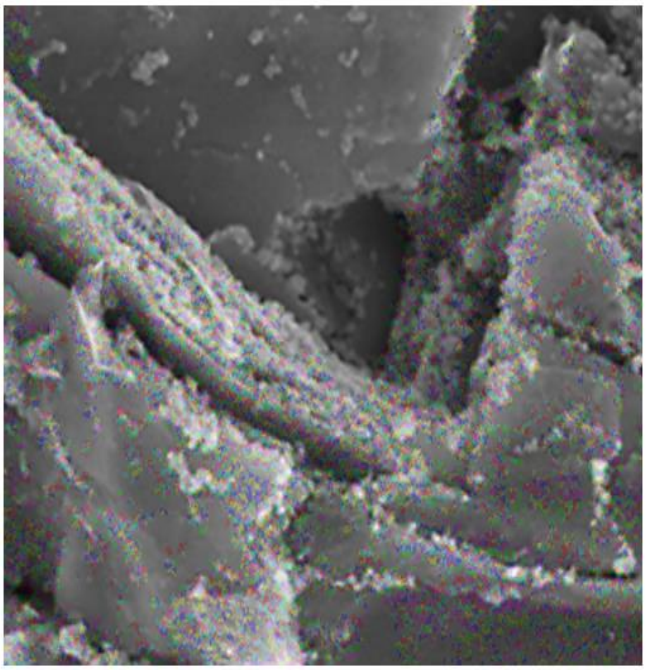

Figure 5: The FESEM images of TiO2/Ti3C2Tx MXene heterostructure NCs after PCD of CBZ in PCI ww (FESEM images size: 100 nm).

3.3.5. The Result of FTIR Analysis

The FTIR spectrum of Ti3C2Tx NCs (black spectrum) (Figure 6a) and TiO2/Ti3C2Tx MXene heterostructure NCs (red spectrum) (Figure 6b) after PCD of CBZ in PCI ww (Figure 6). The main peaks of FTIR spectrum for Ti3C2Tx NCs (black spectrum) was observed at 1080 1/cm, 1051 1/cm, 956 1/cm 563 1/cm wavenumber, respectively (Figure 6a). The main peaks of FTIR spectrum for TiO2/Ti3C2Tx MXene heterostructure NCs (red spectrum) was obtained at 1112 1/cm, 1073 1/cm, 950 1/cm, 740 1/cm and 544 1/cm wavenumber, respectively (Figure 6b).

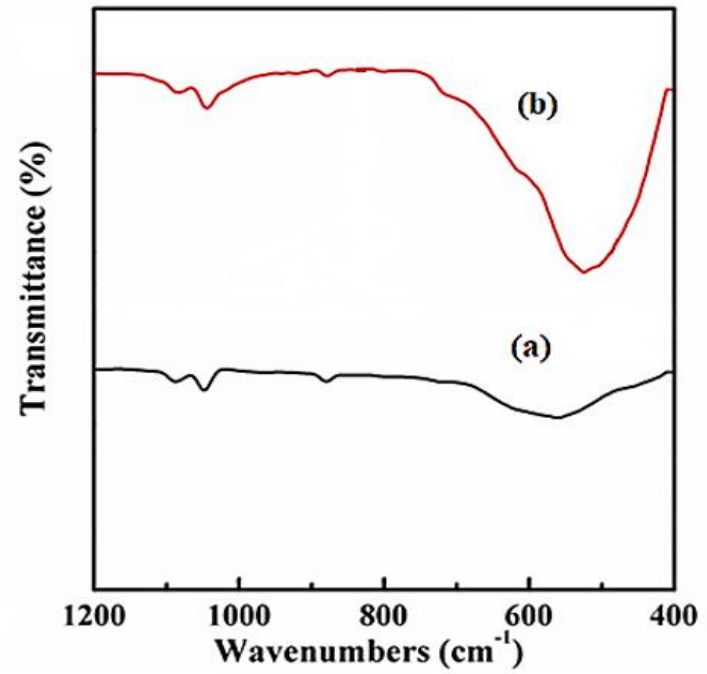

Figure 6: The FTIR spectra of (a) Ti3C2Tx NCs and (b) TiO2/Ti3C2Tx MXene heterostructure NCs after PCD of CBZ in PCI ww.

3.3.6. The Results of TEM Analysis.

The TEM images of TiO2/Ti3C2Tx MXene heterostructure NCs was observed after PCD of CBZ in PCI ww (Figure 7).

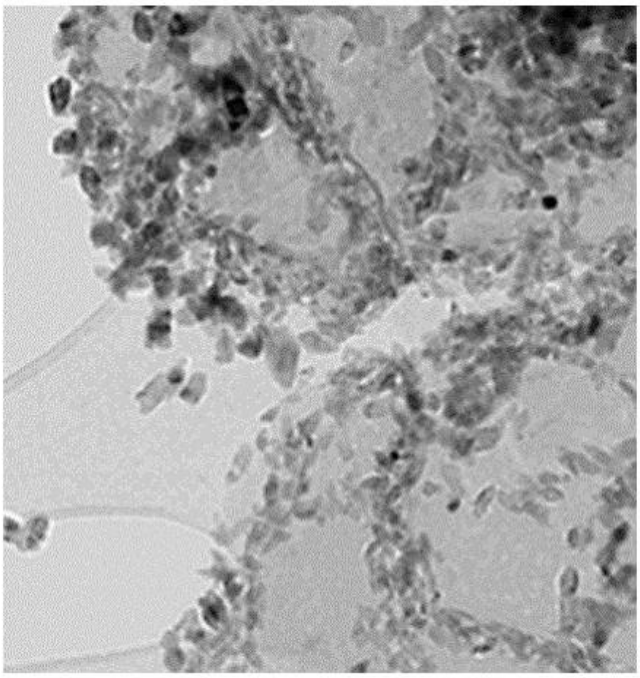

Figure 7: The TEM images of TiO2/Ti3C2Tx MXene heterostructure NCs after PCD of CBZ in PCI ww (TEM images size: 100 nm).

3.4. Effect of Increasing pH Values.

Increasing pH values (3.0, 4.0, 5.0, 6.0, 7.0, 9.0 and 11.0) was examined with PCD for the removal of CBZ in PCI ww, at 300 W UV-vis light and at 25oC (Figure 8). 66.71%, 83.24%, 80.11%, 71.53%, 56.24% and 35.76% CBZ removals was measured at pH=3.0, pH=4.0, pH=6.0, pH=7.0, pH=9.0 and pH=11.0, respectively, at 300 W UV-vis and at 25oC (Figure 8). The maximum 99.34%% CBZ removal was obtained after PCD in PCI ww, at pH=5.0, at 300 W UV-vis and at 25oC, respectively (Figure 8).

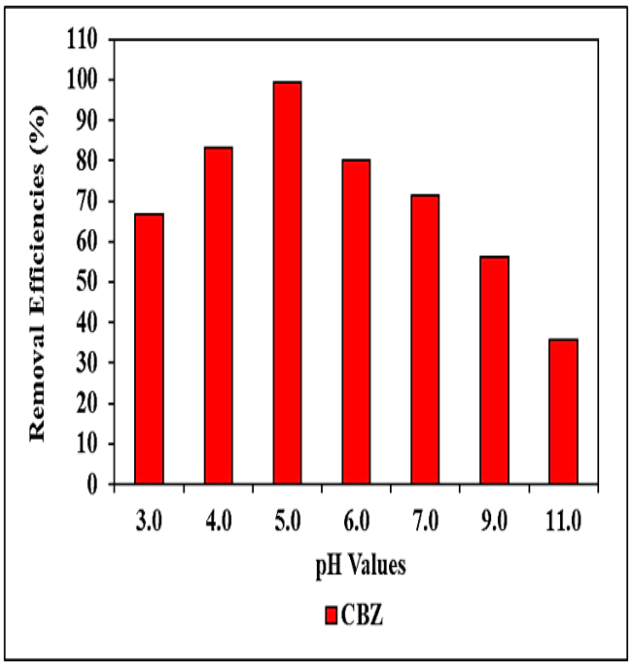

Figure 8: Effect of increasing pH values after PCD in PCI ww for the removals of CBZ, at 300 W UV-vis and at 25oC.

3.5. Effect of Increasing Photocatalytic Degradation Times.

Increasing photocatalytic degradation times (30, 60, 90, 120, 150 and 180 min) were operated with PCD for the removal of CBZ in PCI ww, at 300 W UV-vis, at pH=5.0 and at 25oC, respectively (Figure 9). 44.02%, 60.17%, 78.12%, 85.67% and 92.45% CBZ yields were obtained after 30 min, 60 min, 90 min, 120 min and 150 min, respectively, after PCD in PCI ww, at 300 W UV-vis, at pH=5.0 and at 25oC, respectively (Figure 9). 99.58% CBZ maximum removal was observed after 180 min with PCD in PCI ww, at 300 W UV-vis, at pH=5.0 and at 25oC (Figure 9).

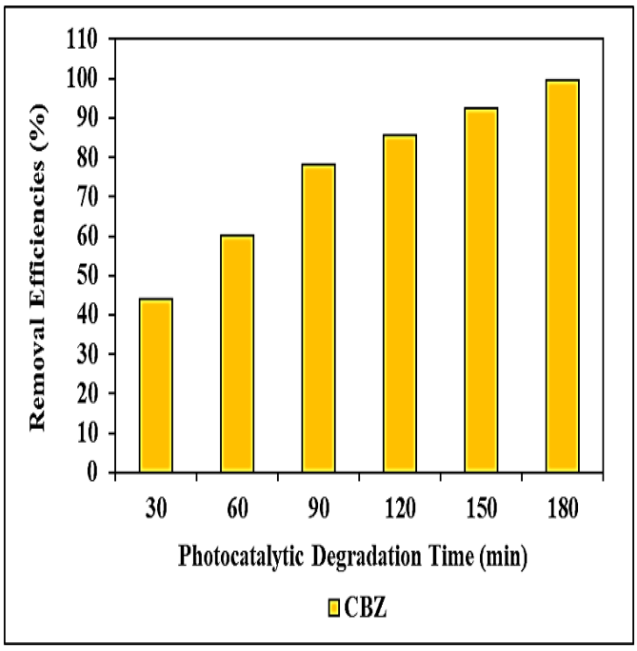

Figure 9: Effect of increasing photocatalytic degradation time after PCD in PCI ww for the removals of CBZ, at 300 W UV-vis, at pH=5.0 and at 25oC.

3.6. Effect of Increasing CBZ Concentrations.

Increasing CBZ concentrations (5, 10, 15 and 20 mg/l) were examined for the efficient CBZ removals in PCI ww with PCD, after 180 min, at 300 W UV-vis, at pH=5.0 and 25oC, respectively (Figure 10). 79.23%, 82.71% and 50.76% CBZ removals were measured after 5 mg/l, 15 mg/l and 20 mg/l CBZ, respectively, after PCD in PCI ww, after 180 min, at 300 W UV-vis, at pH=5.0 and at 25oC, respectively (Figure 10). The maximum 99.42% CBZ removal was obtained at 10 mg/l CBZ with PCD in PCI ww after 180 min, at 300 W UV-vis, at pH=5.0 and at 25oC, respectively (Figure 10).

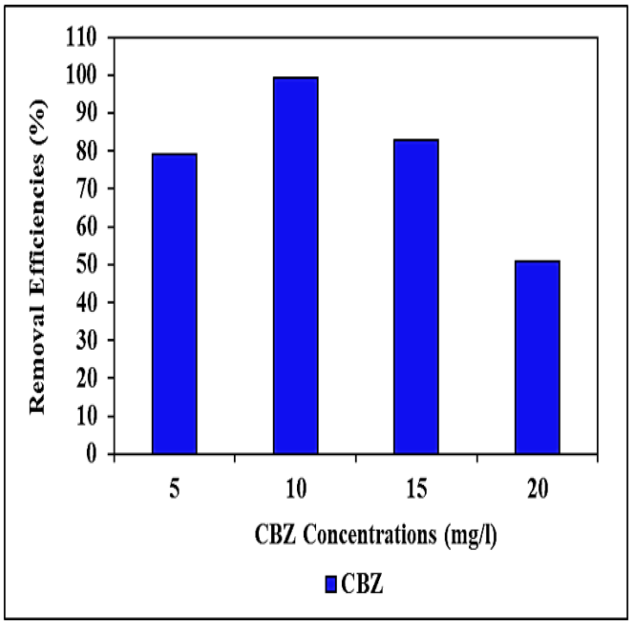

Figure 10: Effect of increasing CBZ concentrations with PCD in PCI ww for the removals of CBZ after 180 min, at 300 W UV-vis, at pH=5.0 and at 25oC, respectively.

3.7. Effect of Increasing TiO2/Ti3C2Tx MXene Heterostructure NCs Photocatalyst Concentrations.

Different TiO2/Ti3C2Tx MXene heterostructure NCs concentrations (5, 10, 20, 40 and 80 mg/l) were operated for the efficient CBZ removals in PCI ww with PCD after 180 min, at 10 mg/l CBZ, at 300 W UV-vis, at pH=5.0 and at 25oC, respectively (Figure 11). 45.29%, 67.44%, 82.74%, 94.36% CBZ yields were found at 5 mg/l, 20 mg/l, 40 mg/l and 80 mg/l TiO2/Ti3C2Tx MXene heterostructure NCs, respectively, after 180 min, at 10 mg/l CBZ, at 300 W UV-vis, at pH=5.0 and at 25oC, respectively (Figure 11). The maximum 99.67% CBZ removal was obtained at 10 mg/l TiO2/Ti3C2Tx MXene heterostructure NCs, after 180 min, at 10 mg/l CBZ, at 300 W UV-vis, at pH=5.0 and at 25oC, respectively (Figure 11).

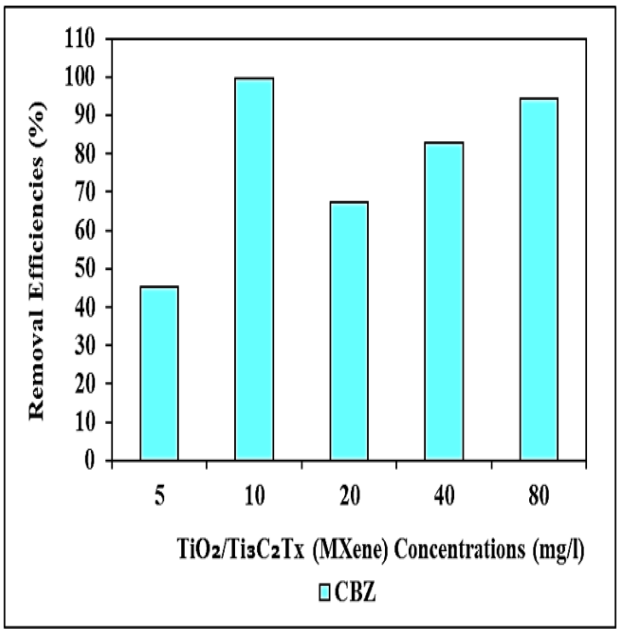

Figure 11: Effect of increasing TiO2/Ti3C2Tx MXene heterostructure NCs photocatalyst concentrations with PCD in PCI ww for the removals of CBZ after 180 min, at 300 W UV-vis, at pH=5.0 and at 25oC, respectively.

Conclusions

The maximum 99.34%% CBZ removal was obtained after PCD in PCI ww, at pH=5.0, at 300 W UV-vis and at 25oC, respectively.

99.58% CBZ maximum removal was observed after 180 min with PCD in PCI ww, at 300 W UV-vis, at pH=5.0 and at 25oC, respectively.

The maximum 99.42% CBZ removal was obtained at 10 mg/l CBZ with PCD in PCI ww after 180 min, at 300 W UV-vis, at pH=5.0 and at 25oC, respectively.

The maximum 99.67% CBZ removal was obtained at 10 mg/l TiO2/Ti3C2Tx MXene heterostructure NCs, after 180 min, at 10 mg/l CBZ, at 300 W UV-vis, at pH=5.0 and at 25oC, respectively.

As a result, the TiO2/Ti3C2Tx MXene heterostructure NCs material in PCI ww was stable in harsh environments such as acidic, alkaline, saline, and then was still effective process. When the amount of contaminant was increased, the TiO2/Ti3C2Tx MXene heterostructure NCs performance was still considerable. Finally, the combination of a simple, easy operation preparation process, cost effective and excellent performance makes this a novel TiO2/Ti3C2Tx MXene heterostructure NCs a promising option during PCD for the removals of CBZ antiepileptic drugs in PCI ww treatment.

Acknowledgement

This research study was undertaken in the Environmental Microbiology Laboratories at Dokuz Eylül University Engineering Faculty Environmental Engineering Department, Izmir, Turkey. The authors would like to thank this body for providing financial support.

References:

1. Khetan, S.K., Collins, T.J. (2007). Human pharmaceuticals in the aquatic environment: A challenge to green chemistry. *Chem. Rev*;107: 2319–2364.
2. Kuster, A., Adler, N. (2014). Pharmaceuticals in the environment: Scientific evidence of risks and its regulation. *Philos. Trans. R. Soc. Lond. Ser. B*; 369: 2013-0587.
3. Patel, M., Kumar, R., Kishor, K., Mlsna, T., Pittman Jr, et al, (2019). D. Pharmaceuticals of emerging concern in aquatic systems: Chemistry, occurrence, effects, and removal methods. *Chem. Rev*.119:3510–3673.
4. Gadipelly, C., Perez-Gonzalez, A., Yadav, G.D., Ortiz, I., Ibanez, R., et al. (2014). Pharmaceutical industry wastewater: Review of the technologies for water treatment and reuse. *Ind. Eng. Chem. Res*; 53: 11571–11592.
5. Bagheri, S., TermehYousefi, A., Do, T.-O. Photocatalytic pathway toward degradation of environmental pharmaceutical pollutants: structure, kinetics and mechanism approach. *Catal. Sci. Technol*; 7: 4548–4569.
6. Calvete, M.J., Piccirillo, G., Vinagreiro, C.S., Pereira, M.M. (2019). Hybrid materials for heterogeneous photocatalytic degradation of antibiotics. *Coord. Chem. Rev*; 395:63–85.
7. Rokesh, K., Sakar, M., Do, T.-O., 2020). Calcium bismuthate (CaBiO3): Apotential sunlight-driven perovskite photocatalyst for the degradation of emerging pharmaceutical contaminants. *ChemPhotoChem*; 4:373–380.
8. Nguyen, C.-C., Nguyen, D.T., Do, T.-O. (2018). A novel route to synthesize C/Pt/TiO2 phase tunable anatase-rutile TiO2 for efficient sunlight-driven photocatalytic applications. *Appl. Catal*. B; 226:46–52.
9. Nguyen, C.C., Vu, N.N., Chabot, S., Kaliaguine, S., Do, T.O. (2017). Role of CxNy-triazine in photocatalysis for efficient hydrogen generation and organic pollutant degradation under solarlight irradiation. *Sol. RRL*; 1:1700012.
10. Vogna, D., Marotta, R., Andreozzi, R., Napolitano, A., d'Ischia, M. (2004). Kinetic and chemical assessment of the UV/H2O2 treatment of antiepileptic drug carbamazepine. *Chemosphere* ;54(4):497-505.
11. Ha, H., Mahanty, B., Yoon, S., Kim, C.-G. (2016). Degradation of the long-resistant pharmaceutical compounds carbamazepine and diatrizoate using mixed microbial culture. *J. Environ. Sci. Heal. Part A*; 51:467–471.
12. Joss, A., Zabaczynski, S., Göbel, A., Hoffmann, B., Löffler, D., et al. (2006). biological degradation of pharmaceuticals in municipal wastewater treatment: Proposing a classification scheme. *Water Res*; 40:1686–1696.
13. Clara, M., Strenn, B., Kreuzinger, N. (2004). Carbamazepine as a possible anthropogenic marker in the aquatic environment: Investigations on the behaviour of carbamazepine in wastewater treatment and during groundwater infiltration. *Water Res*; 38:947–954.
14. Kosjek, T., Andersen, H.R., Kompare, B., Ledin, A., Heath, E. (2009). Fate of carbamazepine during water treatment. *Environ. Sci. Technol*. 43:6256–6261.
15. Khraisheh, M., Kim, J., Campos, L., Al-Muhtaseb, A.H., Al-Hawari, A., et al. (2014). Removal of pharmaceutical and personal care products (PPCPs) pollutants from water by novel TiO2-coconut shell powder (TCNSP) composite. *J. Ind. Eng. Chem*; 20:979–987.
16. Luster, E., Avisar, D., Horovitz, I., Lozzi, L., Baker, M.A., et al. (2017). N-doped TiO2-coated ceramic membrane for carbamazepine degradation in different water qualities. *Nanomaterials (Basel)* ;7(8):206.
17. Carabin, A., Drogui, P., Robert, D. (2015). Photo-degradation of carbamazepine using TiO2 suspended photocatalysts. *J. Taiwan Inst. Chem. Eng*, 54:109–117.
18. Yang, H.G., Sun, C.H., Qiao, S.Z., Zou, J., Liu, G., et al. (2008). Anatase TiO2 single crystals with a large percentage of reactive facets. *Nature*, 453:638–641.
19. Yang, H.G., Liu, G., Qiao, S.Z., Sun, C.H., Jin, Y.G., et al. (2009). Solvothermal synthesis and photoreactivity of anatase TiO nanosheets with dominant {001} facets. *J. Am. Chem. Soc*; 131(11):4078–4083.
20. Gu, L., Wang, J., Cheng, H., Zhao, Y., Liu, L., et al. (2013). One-step preparation of graphenesupported anatase TiO2 with exposed 001 facets and mechanism of enhanced photocatalytic properties. *ACS Appl. Mater. Interfaces*; 5:3085–3093.
21. Zhang, C.J., Pinilla, S., McEvoy, N., Cullen, C.P., Anasori, B., et al. (2017). Oxidation stability of colloidal two-dimensional titanium carbides (MXenes). *Chem. Mater*; 29:4848−4856.
22. Xiong, K., Wang, P., Yang, G., Liu, Z., Zhang, H., et al. (2017). Functional group effects on the photoelectronic properties of MXene (Sc2CT2, T = O, F, OH) and their possible photocatalytic activities. *Sci. Rep*; 7:1–8.
23. Shahzad, A., Rasool, K., Nawaz, M., Miran, W., Jang, J., et al. (2018). Heterostructural TiO2/ Ti3C2Tx (MXene) for photocatalytic degradation of antiepileptic drug carbamazepine. *Chem. Eng. J*; 349:748−755.
24. Shahzad, A., Rasool, K., Miran, W., Nawaz, M., Jang, J., et al. (2018). Mercuric ion capturing by recoverable titanium carbide magnetic nanocomposite. *J. Hazard. Mater*; 344:811−818.
25. Wang, H., Peng, R., Hood, Z.D., Naguib, M., Adhikari, S.P., et al. (2016). Titania composites with 2 D transition metal carbides as photocatalysts for hydrogen production under visible-light irradiation. *ChemSusChem*; 9: 1490–1497.
26. Carp, O., Huisman, C.L., Reller, A. (2004). Photoinduced reactivity of titanium dioxide. *Progr Solid State Chem*; 32: 33–177.
27. Beydoun, D., Amal, R., Low, G., McEvoy, S. (1999). Role of nanoparticles in photocatalysis. *J. Nanoparticle Res*; 1: 439–458.
28. Zhang, H., Sun, S., Shang, X., Guo, B., Li, X., et al. (2022). Ultrafast photonics applications of emerging 2D-Xenes beyond graphene. *Nanophotonics*; 11(7): 1261−1284.
29. Naguib, M., Kurtoglu, M., Presser, V., Lu, J., Niu, J., et al. (2011). Two-dimensional nanocrystals produced by exfoliation of Ti3AlC2. *Adv. Mater*; 23(37): 4248–4253.
30. Jhon, Y.I., Lee, J., Jhon, Y.M., Lee, J.H. (2021). Ultrafast mode-locking in highly stacked Ti3C2Tx MXenes for 1.9-μm infrared femtosecond pulsed lasers. *Nanophotonics*; 10(6): 1741−1751.

31. Xu, B., Gogotsi, Y. (2020). MXenes: from discovery to applications. Adv. Funct. Mater; 30(47).
32. Huang, Y., Yang, H., Zhang, Y., Zhang, Y., Wu, Y., et al. (2019). A safe and fastcharging lithium-ion battery anode using MXene supported Li3VO4. *J. Mater. Chem*. 7(18) :11250−11256.
33. Chen, W., Huang, J., He, Z.-C., Xiong Ji, X., Zhang, Y.-F., et al. (2021). Accelerated photocatalytic degradation of tetracycline hydrochloride over CuAl2O4/g-C3N4 p-n heterojunctions under visible light irradiation. *Separ. Purif. Technol*; 277(8):119-461.
34. Luo, F., X. Feng, X., Zeng, L., Lin, L., Li, X., et al. (2021). In situ simultaneous encapsulation of defective MoS2 nanolayers and sulfur nanodots into SPAN fibers for high-rate sodium-ion batteries. *Chem. Eng. J*; 404:126-430.
35. Ran H., Du H., Ma C., Zhao Y., Feng D., et al. (2021). Effects of A/B-site Co-doping on microstructure and dielectric thermal stability of AgNbO3 ceramics. *Sci. Adv. Mater*; 13:741–747.
36. Xu, L., Guo, W., Zeng, L., Xia, X., Wang, Y., et al. (2021). V3Se4 embedded within N/P co-doped carbon fibers for sodium/potassium ion batteries. *Chem. Eng. J*. 419(6058):129-607.
37. Wang, Y., Liu, J., Chen, X., Kang, B., Wang, H.-E., et al. (2022). Structural engineering of tin sulfides anchored on nitrogen/phosphorus dual-doped carbon nanofibres in sodium/potassium-ion batteries. *Carbon*; 189:46−56.
38. Zhou, W., Li, T., Yuan, M., Li, B., Zhong, S., et al. (2021). Decoupling of inter-particle polarization and intra-particle polarization in core-shell structured nanocomposites towards improved dielectric performance. *Energy Storage Mater*; 42:1−11.
39. Zhou, Y., Qu, Y., Yin, L., Cheng, W., Huang, Y., et al. (2022). Coassembly of elastomeric microfibers and silver nanowires for fabricating ultra-stretchable microtextiles with weakly and tunable negative permittivity. *Compos. Sci. Technol*; 223: 109-415.
40. Hong Ng V.M., Huang, H., Zhou, K., Lee, P.S., Que, W., et al. (2017). Recent progress in layered transition metal carbides and/or nitrides (MXenes) and their composites: synthesis and applications. *J. Mater. Chem. A*; 5: 3039–3068.
41. Guo, J., Peng, Q., Fu, H., Zou, G., Zhang, Q. (2015). Heavy-Metal adsorption behavior of twodimensional alkalization-intercalated MXene by first-principles calculations. *J. Phys. Chem. C*; 119:20923–20930.
42. Shahzad, A., Rasool, K., Miran, W., Nawaz, M., Jang, J., et al. (2017). Two dimensional Ti3C2Tx MXene nanosheets for efficient copper removal from water. *ACS Sustain. Chem. Eng*; 5:11481–11488.
43. Peng, C., Yang, X., Li, Y., Yu, H., Wang, H., et al. (2016). Hybrids of two-dimensional Ti3C2 and TiO2 exposing 001 facets toward enhanced photocatalytic activity. *ACS Appl. Mater. Interfaces*; 8:6051–6060.
44. Cai, T., Wang, L., Liu, Y., Zhang, S., Dong, W., et al. (2018). Ag3PO4/Ti3C2 MXene interface materials as a Schottky catalyst with enhanced photocatalytic activities and anti-photocorrosion performance. *Appl. Catal., B*; 239:545−554.
45. Lipps, W.C., Braun-Howland, E.B., Baxter, T.E. (2022). Standard Methods for the Examination of Water and Wastewater. (24th. Edition). American Public Health Association (APHA), American Water Works Association (AWWA), Water Environment Federation (WEF), Elevate Your Standards. American Public Health Association 800 I Street, NW Washington DC: 20001-3770, USA,
46. Olthof, M., Eckenfelder, W.W. (1976). Coagulation of textile wastewater. *Text. Chem. Color*; 8:18-22.
47. Eckenfelder, W.W., (1989). Industrial Water Pollution Control (2nd ed), Signapore: McGraw-Hill Inc.
48. Zar, J.H. (1984). Biostatistical analysis, Prentice-Hall, Englewood Cliffs.
49. Statgraphics Centurion XV, sofware, StatPoint Inc, Statgraphics Centurion XV, Herndon, VA, USA, (2005).
50. Halim, J., Cook, K.M., Naguib, M., Eklund, P., Gogotsi, Y., et al. (2016). X-ray photoelectron spectroscopy of select multi-layered transition metal carbides (MXenes). *Appl. Surf. Sci*; 362:406–417.
51. Mora-Seró, I., Bisquert, J. (2003). Fermi level of surface states in TiO2 nanoparticles. *Nano Lett*; 3:945–949.
52. Zhao, Z., Li, Z., Zou, Z. (2010). Surface properties and electronic structure of low-index stoichiometric anatase TiO2 surfaces. *J. Phys. Condens. Matter*; 22:175008.
53. Nawaz, M., Miran, W., Jang, J., Lee, D.S. (2017). One-step hydrothermal synthesis of porous 3D reduced graphene oxide/TiO2 aerogel for carbamazepine photodegradation in aqueous solution. *Appl. Catal. B Environ*; 203:85–95.
54. Xu, J., Li, L., Guo, C., Zhang, Y., Meng, W. (2013). Photocatalytic degradation of carbamazepine by tailored BiPO4: efficiency, intermediates and pathway. Appl. Catal. B Environ; 130–131:285–292.